1-2023

# Spatial heterogeneity in sediment and carbon accretion rates within a seagrass meadow correlated with the hydrodynamic intensity

Jiarui Lei

Rachel Schaefer

Phil Colarusso

Alyssa Novak

Juliet C. Simpson

*See next page for additional authors*



10.1016/j.scitotenv.2022.158685

Lei, J., Schaefer, R., Colarusso, P., Novak, A., Simpson, J. C., Masqué, P., & Nepf, H. (2023). Spatial heterogeneity in sediment and carbon accretion rates within a seagrass meadow correlated with the hydrodynamic intensity. *Science of The Total Environment*, 854, Article 158685.
https://doi.org/10.1016/j.scitotenv.2022.158685

Science of the Total Environment 854 (2023) 158685

Contents lists available at ScienceDirect

Science of the Total Environment

journal homepage: www.elsevier.com/locate/scitotenv

# Spatial heterogeneity in sediment and carbon accretion rates within a seagrass meadow correlated with the hydrodynamic intensity

Jiarui Lei [a,b], Rachel Schaefer [a,*], Phil Colarusso [c], Alyssa Novak [d], Juliet C. Simpson [e], Pere Masqué [f,g,h], Heidi Nepf [a]

[a] Department of Civil and Environmental Engineering, Massachusetts Institute of Technology, 77 Massachusetts Avenue, Room 1-290, Cambridge, MA 02139, United States of America
[b] Department of Civil and Environmental Engineering, National University of Singapore, Block E1A, #07-03, No. 1 Engineering Drive 2, 117576, Singapore
[c] U.S. Environmental Protection Agency, 5 Post Office Square, Suite 100, Boston, MA 02109, United States of America
[d] Department of Earth & Environment, Boston University, 685 Commonwealth Avenue, Room 130, Boston, MA 02215, United States of America
[e] MIT Sea Grant College Program, Massachusetts Institute of Technology, 77 Massachusetts Avenue, Room NW98-151, Cambridge, MA 02139, United States of America
[f] School of Science and Centre for Marine Ecosystems Research, Edith Cowan University, 270 Joondalup Drive, Joondalup 6027, Australia
[g] International Atomic Energy Agency Environment Laboratories, 4 Quai Antoine 1er, B.P. 800, 98012 Monaco Cedex, Principality of Monaco
[h] Department of Physics, Institute of Environmental Science and Technology, Universitat Autònoma de Barcelona, Edifici C, 08193, Bellaterra (Cerdanyola del Vallès), Barcelona, Spain

## HIGHLIGHTS

- Spatial gradients in carbon and wave intensity were compared across a *Zostera marina* (L.) meadow.
- Higher near-bed turbulence was correlated with lower sediment and carbon accretion rates.
- Storm events may dominate resuspension and therefore carbon storage.
- Wave dissipation by the seagrass meadow influenced the spatial variation in carbon.

## GRAPHICAL ABSTRACT

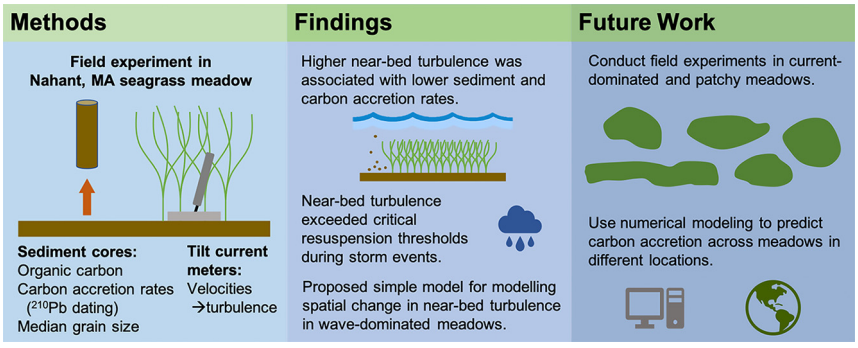


## ARTICLE INFO

Editor: Jan Vymazal

*Keywords:*
*Zostera marina*
Carbon accretion
Turbulent kinetic energy
Resuspension

## ABSTRACT

The majority of the carbon stored in seagrass sediments originates outside the meadow, such that the carbon storage capacity within a meadow is strongly dependent on hydrodynamic conditions that favor deposition and retention of fine organic matter within the meadow. By extension, if hydrodynamic conditions vary across a meadow, they may give rise to spatial gradients in carbon. This study considered whether the spatial gradients in sediment and carbon accretion rates correlated with the spatial variation in hydrodynamic intensity within a single meadow. Field measurements were conducted in three depth zones across a *Zostera marina* L. (eelgrass) meadow in Nahant Harbor, Massachusetts. Four sediment cores were collected in each zone, including one outside the meadow (control) and three within the meadow at increasing distances from the nearest meadow edge. Sedimentation and carbon accretion rates were estimated by combining the measurements of dry bulk density, organic carbon fraction (%OC), $^{210}$Pb, and $^{226}$Ra. Tilt current meters measured wave velocities within each zone, which were used to estimate turbulent kinetic energy (*TKE*). Both sediment and carbon accretion rates exhibited spatial heterogeneity across the meadow, which were correlated with the spatial variation in near-bed *TKE*. Specifically, both accretion rates increased with decreasing

* Corresponding author.
*E-mail addresses:* jlei@nus.edu.sg (J. Lei), rbs@mit.edu (R. Schaefer), colarusso.phil@epa.gov (P. Colarusso), abnovak@bu.edu (A. Novak), simpsonj@mit.edu (J.C. Simpson), p.masque@ecu.edu.au (P. Masqué), hmnepf@mit.edu (H. Nepf).

http://dx.doi.org/10.1016/j.scitotenv.2022.158685
Received 20 April 2022; Received in revised form 17 August 2022; Accepted 7 September 2022
Available online 13 September 2022

*TKE*, which was consistent with diminished resuspension associated with lower *TKE*. A method is proposed for using spatial gradients in hydrodynamic intensity to improve the estimation of total meadow accretion rates.

## 1. Introduction

Seagrass meadows are global hotspots for carbon storage (e.g., Kennedy et al., 2010; Duarte et al., 2010; Fourqurean et al., 2012). However, carbon stocks vary significantly between different seagrass sites. For example, Lavery et al. (2013) reported an 18-fold range in carbon stock measured across seventeen different seagrass habitats (260 to 4800 g C $m^{-2}$). Similarly, Serrano et al. (2014) observed a 14-fold difference in carbon stock over a 10-fold difference in water depth, which they attributed to gradients in light availability. The variability in carbon stock is a major source of uncertainty in assessing global seagrass carbon stocks; therefore, there is a need to understand the factors driving this variability (Lavery et al., 2013; Serrano et al., 2014).

More than 50 % of the carbon stored in seagrass sediments originates outside the meadow (known as allochthonous carbon), so that the carbon storage capacity within a meadow is dependent on hydrodynamic conditions that favor deposition and retention of fine organic matter (e.g., Gacia and Duarte, 2001; Gacia et al., 1999; Kennedy et al., 2010). Therefore, hydrodynamic conditions should help to explain differences in measured seagrass carbon stocks and burial rates (Granata et al., 2001; Gruber and Kemp, 2010). For example, Oreska et al. (2017) observed that sediment organic carbon increased with distance from the meadow edge and attributed this to the attenuation of current by meadow drag forces. Ricart et al. (2020) attributed an increase in seagrass meadow carbon stocks between the lower and upper regions of an estuary to a decrease in hydrodynamic intensity. Similarly, Novak et al. (2020) observed higher carbon stocks at sites with lower wave and current exposure.

The correlation between hydrodynamic intensity and carbon stock is likely due to sediment resuspension. For example, Dahl et al. (2018) showed that sediment resuspension within a meadow led to a loss of carbon from the surface sediment. Previous studies have linked resuspension within a meadow to near-bed turbulent kinetic energy (*TKE*). Resuspension occurs when *TKE* increases above a critical magnitude, which depends on the median sediment grain size (e.g., Tinoco and Coco, 2018; Tang et al., 2019). For a unidirectional current interacting with a submerged meadow, spatial gradients in *TKE* have been correlated with spatial gradients of net deposition. Specifically, when a unidirectional current encounters a submerged meadow, the hydrodynamic drag generated by the meadow causes the within-meadow current velocity and *TKE* to decrease with distance from the leading edge (e.g., Chen et al., 2013; Lei and Nepf, 2021). Zhang et al. (2020) observed that net deposition increased with distance from the meadow leading edge, correlated with the progressive decrease in *TKE*.

In addition to reducing current velocity, seagrass meadows also attenuate wave energy, which may diminish near-bed wave velocity (e.g., Fonseca and Cahalan, 1992; Mendez and Losada, 2004; Infantes et al., 2012; Lei and Nepf, 2019). The interaction between the wave velocity and the seagrass sheath generates turbulence near the bed (Zhang et al., 2018), which can trigger sediment resuspension (Tinoco and Coco, 2018; Tang et al., 2019). Combining these effects, Tang et al. (2019) predicted the meadow size needed to diminish wave energy enough to eliminate wave-induced resuspension and enhance particle retention.

Building on the studies described above, the present study used field observations at a wave-dominated site to examine the connection between sediment and carbon accretion rates, wave velocity, and *TKE* within a single meadow. An understanding of how resuspension may impose spatial gradients on carbon accretion could improve the assessment of carbon credit for seagrass meadows, as well as provide guidelines to optimize long-term carbon accretion potential. To this end, a method is proposed for using predicted gradients in hydrodynamic exposure to improve estimates of meadow-scale carbon accretion rates.

## 2. Methods

### 2.1. Meadow and sediment characteristics

This study was conducted in a meadow of *Zostera marina* in Nahant Harbor, Massachusetts (Fig. 1), which is a wave-dominated site. Based on isotopic signature analysis, the carbon in this meadow has a significant allochthonous fraction (Fig. 8 in Novak et al., 2020), so that the accretion rate of organic carbon was expected to be influenced, at least in part, by hydrodynamic conditions favorable for its retention. Meadow boundaries were delineated through a boat survey. In Fig. 1, the outer edge of the meadow is shown with pink line segments, which enclose 14.3 acres (0.06 $km^2$). A denser inner region (5.2 acres, 0.02 $km^2$) is shown with green line segments. The meadow was divided into three depth zones, which were expected to experience different hydrodynamic conditions: Shallow (mean water depth = 2.2 m), Mid (mean depth = 3.2 m), and Deep (mean depth = 6.2 m). Mean water depths were measured with diver depth gauges and corrected for tidal phase. In July 2020, within each of the three depth zones, three cores were extracted within the meadow and a fourth reference core was collected from the adjacent bare bed, resulting in a total of 12 cores. A 50-cm core barrel with 7-cm diameter was manually driven to the point of refusal, which ranged from 24 cm to 30 cm. The core locations are shown in Fig. 1.

After the cores were extracted, they were capped underwater and kept vertical during transport from the extraction sites to the beach. Depending on the core length, the cores were extruded into 22 to 25 sections, with 1-cm increments from 0 to 20 cm and 2-cm increments from 20 to 30 cm. The core subsamples were stored in Ziploc bags on ice in coolers and transported to the Novak Lab at Boston University in Boston, Massachusetts. Samples were put into a drying oven at 60 °C for seven days or until they attained a constant weight. The dry bulk density of each slice was calculated by dividing the dry mass of the sample by the volume. Next, the sediment samples were divided in half with a sediment splitter. One half of each sample was placed in a muffle furnace at 450 °C for 16 h to determine the percent organic matter content (%OM) using the loss-on-ignition method (Howard et al., 2014). Percent organic carbon (%OC) was calculated assuming a linear dependence on %OM based on data from sites across New England reported in Novak et al. (2020). %OM, %OC, and bulk dry density were averaged over the top 15 cm of each core. These parameters showed no trends with depth into the cores. The grain size distribution was measured by combining samples from the top 5 cm and sieving from 0.5 mm to 0.0625 mm. The median grain size was calculated from the grain size distribution.

The second half of each sediment sample was shipped to Edith Cowan University in Joondalup, Australia for $^{210}$Pb analysis to determine sediment accumulation rates (*SAR*) and mass accumulation rates (*MAR*). $^{210}$Pb was determined by analyzing $^{210}$Po using alpha spectrometry after the addition of $^{209}$Po as an internal tracer and digestion in acid media using an analytical microwave (Sanchez-Cabeza et al., 1998). Gamma spectrometry measurements determined the concentration of $^{226}$Ra in selected samples along each core. The excess $^{210}$Pb was defined as the difference between the total $^{210}$Pb and $^{226}$Ra (i.e., supported $^{210}$Pb). Using the $^{210}$Pb concentration profiles, an average *MAR* was calculated using the Constant Flux and Constant Sedimentation (CF: CS, applied piecewise) model (e.g., Krishnaswami et al., 1971; Arias-Ortiz et al., 2018). Cores that indicated significant mixing were not analyzed for *MAR*. The carbon accretion rate (*CAR*) was estimated by combining *MAR* with %OC (see Table 1).

On the same day the cores were extracted, the shoot density was measured near each core site with three randomly placed quadrats (25 cm x 25 cm). The leaf width, length, sheath length, number of leaves, and shoot biomass were measured for five selected shoots within each quadrat.

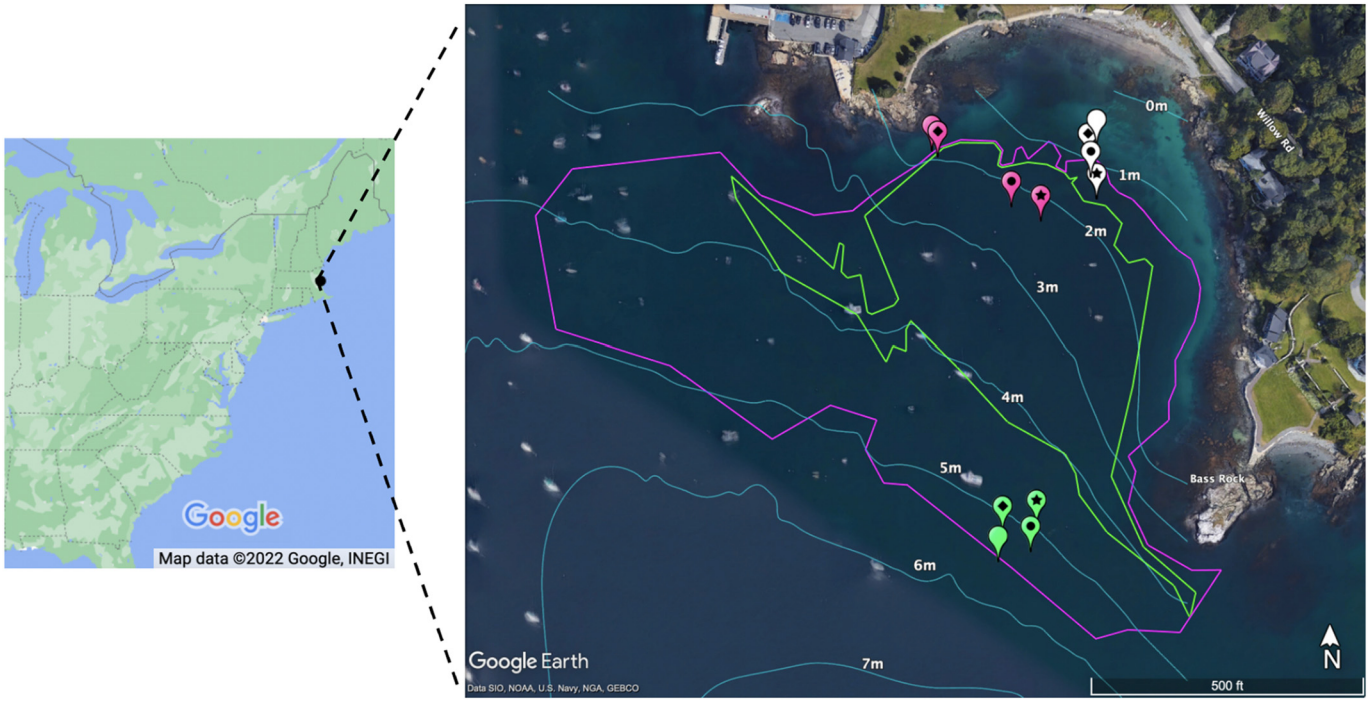


**Fig. 1.** The field site in Nahant Harbor, Massachusetts, on the East Coast of the United States. Four cores were collected in each of three depth zones; three within the meadow at increasing distance from the nearest meadow edge, numbered 1 (diamonds), 2 (circles), 3 (stars), respectively, and one reference core outside of the meadow ("Ref," blank markers). White, pink, and green denote the Shallow, Mid, and Deep depth zones, respectively. Green and magenta outlines show the regions of dense (shoot density > 200 $m^{-2}$) and sparse (shoot density < 200 $m^{-2}$) vegetation mapped using boat surveys in 2014. The bathymetry surveyed in 2014 is indicated by labeled blue contour lines.

Leaf area index (*LAI*) was calculated as the product of the mean leaf area per shoot (sheath included) and shoot density (see Table 1).

### 2.2. Velocity and turbulence

In August 2021, six tilt current meters (TCMs) designed and manufactured by Lowell Instruments, LLC (East Falmouth, Massachusetts) were deployed in Nahant Harbor at Shallow(Ref), Shallow1, Mid(Ref), Mid2, Deep (Ref), and Deep3. The TCM deployment sites were chosen because the extracted sediment cores at these sites yielded mass accretion rates from the $^{210}$Pb analysis. Each TCM consisted of a cylindrical housing tethered by a short cord to an anchor, which in this study was a 20-lb, 12-in by 12-in by 2-in square concrete paving stone. In the absence of water motion, the long axis of the cylinder is vertical. The cylinder tilts in response to the wave and current velocities. An accelerometer and magnetometer within the cylinder measure the degree and direction of tilt, which is converted through factory calibration coefficients into velocity and heading. Data were recorded at 16 Hz for 60-s bursts every 5 min at all sites except Shallow(Ref). Due to concerns about boat traffic, the instrument at Shallow (Ref) recorded at 16 Hz continuously for 24 h, at which point it was removed. The remaining TCMs were deployed for a minimum of two weeks. All TCMs were fully submerged during their deployment. The total height of each TCM setup was 33 cm, which was less than the observed meadow height at all sites, confirmed by measured shoot height and GoPro footage recorded at the Deep3 site. Although TCMs are primarily marketed to record unidirectional flow, a comparison with an acoustic Doppler velocimeter (Nortek Vectrino) in an experimental channel confirmed their ability to record wave velocity (see Fig. A.1 in the Supporting Information). The average root-mean-squared velocity, $U_{RMS}$, was estimated over each 1-h interval, from which wave velocity amplitude was defined as $U_w = 2^{1/2}U_{RMS}$.

**Table 1**
Summary of measured meadow structure and sediment characteristics averaged over the top 15 cm of the sediment cores, consistent with the depth of cores that was used to assess *MAR* and *SAR* (Fig. 2). Standard deviations among quadrat samples (shoot density) and over sediment profiles (dry bulk density, %OC, *SAR*) are reported. Derived quantities (*LAI*, organic carbon, *CAR*) include propagated uncertainty.

| | Distance to edge | Mean water depth | Dry bulk density | %OC | Shoot density | *LAI* | Organic carbon | Median grain size | *MAR* | *SAR* | *CAR* |
|---|---|---|---|---|---|---|---|---|---|---|---|
| | m | m | g/cm$^3$ | % | m$^2$ | m$^2$/m$^2$ | g C/cm$^3$ | mm | g/cm$^2$ yr | mm/yr | g C/m$^2$ yr |
| D1 | 11 | 6.3 | 1.54 ± 0.13 | 0.33 ± 0.08 | 91 ± 46 | 0.9 ± 0.5 | 0.0051 ± 0.0012 | 0.11 | | | 15 ± 5 |
| D2 | 19 | 6.2 | 1.53 ± 0.14 | 0.35 ± 0.04 | 59 ± 9 | 0.69 ± 0.11 | 0.0054 ± 0.0007 | 0.11 | | | 16 ± 4 |
| D3 | 29 | 6.0 | 1.45 ± 0.20 | 0.42 ± 0.07 | 85 ± 18 | 0.74 ± 0.16 | 0.0062 ± 0.0013 | 0.11 | 0.45 ± 0.10 | 3.1 ± 0.7 | 19 ± 5 |
| DR | 1 | 6.5 | 1.41 ± 0.19 | 0.29 ± 0.07 | | | 0.0040 ± 0.011 | 0.12 | | | |
| M1 | 5 | 3.0 | 1.21 ± 0.19 | 0.68 ± 0.25 | 261 ± 9 | 3.04 ± 0.11 | 0.008 ± 0.003 | 0.10 | | | 14 ± 6 |
| M2 | 54 | 3.3 | 1.36 ± 0.17 | 0.47 ± 0.16 | 331 ± 76 | 7.9 ± 1.8 | 0.007 ± 0.002 | 0.10 | 0.21 ± 0.04 | 1.6 ± 0.3 | 10 ± 4 |
| M3 | 72 | 3.3 | 1.39 ± 0.16 | 0.47 ± 0.11 | 261 ± 65 | 4.3 ± 1.1 | 0.0065 ± 0.0017 | 0.09 | | | 10 ± 3 |
| MR | 1 | 3.0 | 1.36 ± 0.14 | 0.21 ± 0.03 | | | 0.0028 ± 0.0005 | 0.10 | | | |
| S1 | 11 | 2.0 | 1.41 ± 0.18 | 0.21 ± 0.08 | 240 ± 48 | 3.7 ± 0.7 | 0.0030 ± 0.0011 | 0.10 | 0.12 ± 0.02 | 0.90 ± 0.18 | 2.5 ± 1.0 |
| S2 | 19 | 2.3 | 1.41 ± 0.17 | 0.20 ± 0.04 | 251 ± 76 | 4.8 ± 1.4 | 0.0027 ± 0.0006 | 0.09 | | | 2.3 ± 0.6 |
| S3 | 29 | 2.6 | 1.33 ± 0.39 | 0.23 ± 0.05 | 176 ± 55 | 1.2 ± 0.4 | 0.0031 ± 0.0011 | 0.10 | | | 2.8 ± 0.8 |
| SR | 8 | 1.7 | 1.33 ± 0.22 | 0.29 ± 0.08 | | | 0.0039 ± 0.0013 | 0.07 | | | |

Velocity records confirmed that this is a wave-dominated site, with wave velocity much larger than time-mean velocity. Tidal elevations at high and low tides were obtained from Nahant US Harbors data.

Because previous studies have correlated resuspension with near-bed turbulence, the measured near-bed wave velocity was used to estimate near-bed turbulence. Turbulence is generated by the interaction of the wave velocity with the bed and with the relatively stiff sheath of each seagrass shoot (Zhang et al., 2018; Tang et al., 2019). The vegetation-generated turbulent kinetic energy per fluid mass (*TKE*) can be predicted from a model based on the conversion of wave kinetic energy to *TKE* by canopy drag (Tanino and Nepf, 2008; Tang et al., 2019). The bed-generated turbulence is linearly proportional to the bed-generated shear stress, $\tau_w = \rho f_w {U_w}^2/2$, in which $f_w$ is a wave friction factor (Tang et al., 2019). The sum of these predicts the total near-bed *TKE*:

$$\text{near}-\text{bed TKE} = \underbrace{\delta\left(C_D\frac{n_s b^2}{2(1-\phi)}\right)^{\frac{2}{3}}U_{RMS}^2}_{\text{vegetation}-\text{generated turbulence}} + \underbrace{C_{b,w}U_{RMS}^2}_{\text{bed}-\text{generated turbulence}}, \quad (1)$$

in which the scale factor $\delta = 1.2 \pm 0.2$ is an average from two previous studies (Tanino and Nepf, 2008; Tang et al., 2019). $n_s$ is the number of shoots per bed area. $b$ is the sheath diameter (see Section 3.2 in Zhang et al., 2018), which was assumed to be equal to the leaf width. Since the sheath has a nearly cylindrical geometry, the near-bed solid volume fraction $\phi = \frac{\pi}{4} n_s b^2$. $C_D$ (=1.2) is the sheath drag coefficient, based on cylinder drag measurements in Keulegan and Carpenter (1958). The bare-bed scale factor $C_{b,w}$, defined by measurements over bare bed, is a function of bed roughness. We used a value measured by Tang et al. (2019), $C_{b,w} = 0.02 \pm 0.01$ for $d_{50} = 85$ μm, which is close to the sediment grain size at Nahant ($d_{50} = 100$ μm).

The critical *TKE* threshold was estimated using the critical velocity for bare beds, modified for meadows (Tang et al., 2019). First, Komar and Miller (1973) showed that for a median grain size $d_{50}$ <0.05 cm, the critical wave velocity for a bare bed, $U_{w,c,b}$, is given by

$$\frac{\rho {U_{w,c,b}}^2}{(\rho_s - \rho) g d_{50}} = 0.3\sqrt{\frac{2A_{w,c,b}}{d_{50}}}, \quad (2)$$

in which $\rho_s$ is the sediment density, $g$ is the gravitational acceleration, $A_{w,c,b} = U_w T/(2\pi)$ is the critical wave excursion, and $T$ is the wave period. The critical RMS wave velocity is then, $U_{RMS,c,b} = U_{w,c,b}/\sqrt{2}$.The critical velocity threshold within the meadow is reduced, relative to the bare bed, due to the contribution from vegetation-generated turbulence. Specifically, the critical rms wave velocity in a meadow, $U_{RMS,c,v}$, is (Tang et al., 2019)

$$\frac{U_{RMS,c,v}}{U_{RMS,c,b}} = \frac{1}{\sqrt{1 + \frac{\delta^2}{C_{b,w}}\left(\frac{2C_D}{\pi}\right)^{\frac{2}{3}}\left(\frac{\phi}{1-\phi}\right)^{\frac{2}{3}}}}. \quad (3)$$

The critical RMS wave velocity can be used in Eq. (1) to estimate the critical *TKE*. We emphasize that this prediction is for near-bed, wave-generated turbulence. This is our focus because near-bed turbulence has been shown to correlate with resuspension (Tang et al., 2019). The vertically-averaged, wave-driven turbulence within a meadow is much smaller, because the turbulence decays sharply with distance from the bed (see Fig. 3(f) in Zhang et al., 2018). This is because bed-generated turbulence is limited by a thin wave-boundary-layer, and because the seagrass leaves can easily move with the waves, reducing relative motion and thus reducing vegetation-generated turbulence above the sheath region (see discussions in Zhang et al., 2018 and Tang et al., 2019).

## 3. Results and discussion

### 3.1. Meadow structure and sediment characteristics

The measured meadow structure and sediment characteristics are summarized in Table 1. The shoot density was highest in the Mid zone and lowest in the Deep zone. The measured leaf width averaged over all quadrats was $b = 0.47 \pm 0.09$ cm. The median grain size was comparable across the meadow, increasing by just 20 % between the Shallow and Deep zones. The nearly uniform grain size across the meadow can be attributed to a common source of suspended material, derived from a nearby marsh.

In the Deep zone, the total $^{210}$Pb concentrations decreased with depth in the meadow cores (green, blue, and red symbols in Fig. 2(a)) from around 25 Bq/kg at the surface down to a constant of 14.9 ± 1.6 Bq/kg below 10 to 12 cm. Based on the Deep1, Deep2, and Deep3 cores, the mass accretion rate was $MAR = 0.45 \pm 0.01$ g cm$^{-2}$ yr$^{-1}$, and the sedimentation accretion rate was $SAR = 3.1 \pm 0.7$ mm/yr (Fig. 2(a)). In the meadow Mid zone, $MAR = 1.6 \pm 0.3$ g cm$^{-2}$ yr$^{-1}$ and $SAR = 1.6 \pm 0.3$ mm/yr based on the Mid2 core (Fig. 2(b)). In the meadow Shallow zone, $MAR = 0.90 \pm 0.18$ g cm$^{-2}$ yr$^{-1}$ and $SAR = 0.90 \pm 0.18$ mm/yr based on the Shallow1 core (Fig. 2(c)).

### 3.2. Velocity, turbulent kinetic energy, and sediment accumulation rate

Wind speeds observed during the deployment were typical of historical wind conditions (based on records from the weather station at the Boston Logan International Airport), so that the observed spatial trends in hydrodynamic intensity were considered to be representative of the long-term conditions that produced the recorded spatial trend in mass accretion. Power spectra of velocity records indicated dominant wave periods between 6 and 10 s, which was consistent with historical data from the National Oceanic and Atmospheric Administration National Data Buoy Center (NOAA NDBC) Station 44,013 buoy in Massachusetts Bay. For this wave period and local depth range, the near-bed wave velocity is sensitive to depth, specifically increasing as depth decreases. As a result, the magnitude of the near-bed $U_{RMS}$ was correlated with the tidal phase (Fig. 3), with peak $U_{RMS}$ values associated with low tide (vertical gray lines in Fig. 3), which was particularly evident at the Shallow1 site (black curve in Fig. 3). Over the two-week deployment, the average RMS velocity was highest at the Shallow1 site (6.6 cm/s), less at the Mid2 site (5.3 cm/s), and smallest at the Deep3 site (4.7 cm/s). Within each depth zone, the RMS velocity measured just outside the meadow differed from the in-meadow velocity by <10 % (data not shown). That is, the meadow did not locally diminish the wave velocity within the meadow compared to just outside of the meadow. This was consistent with the prediction of wave velocity attenuation described in Lowe et al. (2005). Specifically, based on the meadow density and wave period, the in-canopy wave velocity attenuation factor $\alpha \approx 1$ for all depth zones. Large wave events on Days 2, 7, and 13 were correlated with stormy weather reported on Logan International Airport wind speed and precipitation data.

The near-bed *TKE* was estimated from measured $U_{RMS}$ using Eq. (1). We considered the strong wave conditions observed during low tides on Days 2, 7, and 13, referred to as Storms 1, 2, and 3. Consistent with the spatial variation in $U_{RMS}$ in Fig. 3, the Shallow1 site experienced the highest *TKE* while the Deep3 site experienced the lowest *TKE* (Fig. 4). The critical *TKE* threshold for sediment resuspension (based on Eqs. (1), (2), and (3)) are indicated with horizontal lines in Fig. 4(a). During Storm 3, the *TKE* at the Shallow1 and Mid2 sites significantly exceeded the thresholds, while the thresholds were barely crossed at the Shallow1 and Mid2 sites during Storms 1 and 2. Based on this, we infer that events with velocity magnitude similar to or greater than that of Storm 3 control the spatial distribution of sediment carbon within the meadow. With this in mind, in the next phases of analysis we focus on Storm 3.

The *SAR* (Table 1, Fig. 4(b)) varied inversely with near-bed *TKE* during Storm 3, which can be explained by resuspension triggered by near-bed turbulence, i.e., resuspension diminished particle retention and thus sediment

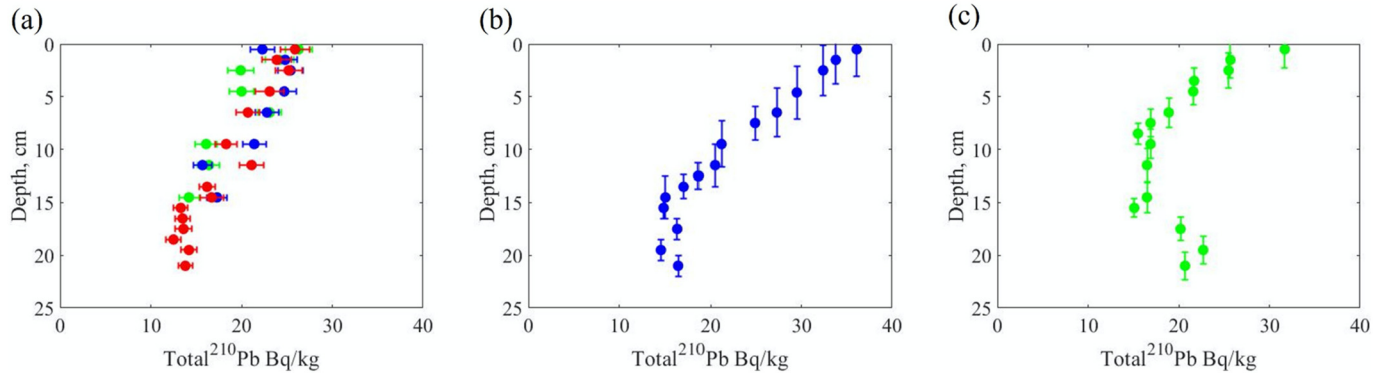


**Fig. 2.** Total $^{210}$Pb and $^{226}$Ra versus depth from the surface of the meadow sediment cores for the (a) Deep zone, (b) Mid zone, and (c) Shallow zone. Only profiles without mixing from which *SAR* and *MAR* were determined are included. Colors correspond to the site distance from the nearest edge of the meadow. Green, blue, and red denote meadow sites at increasing distances from the nearest edge of the meadow, respectively.

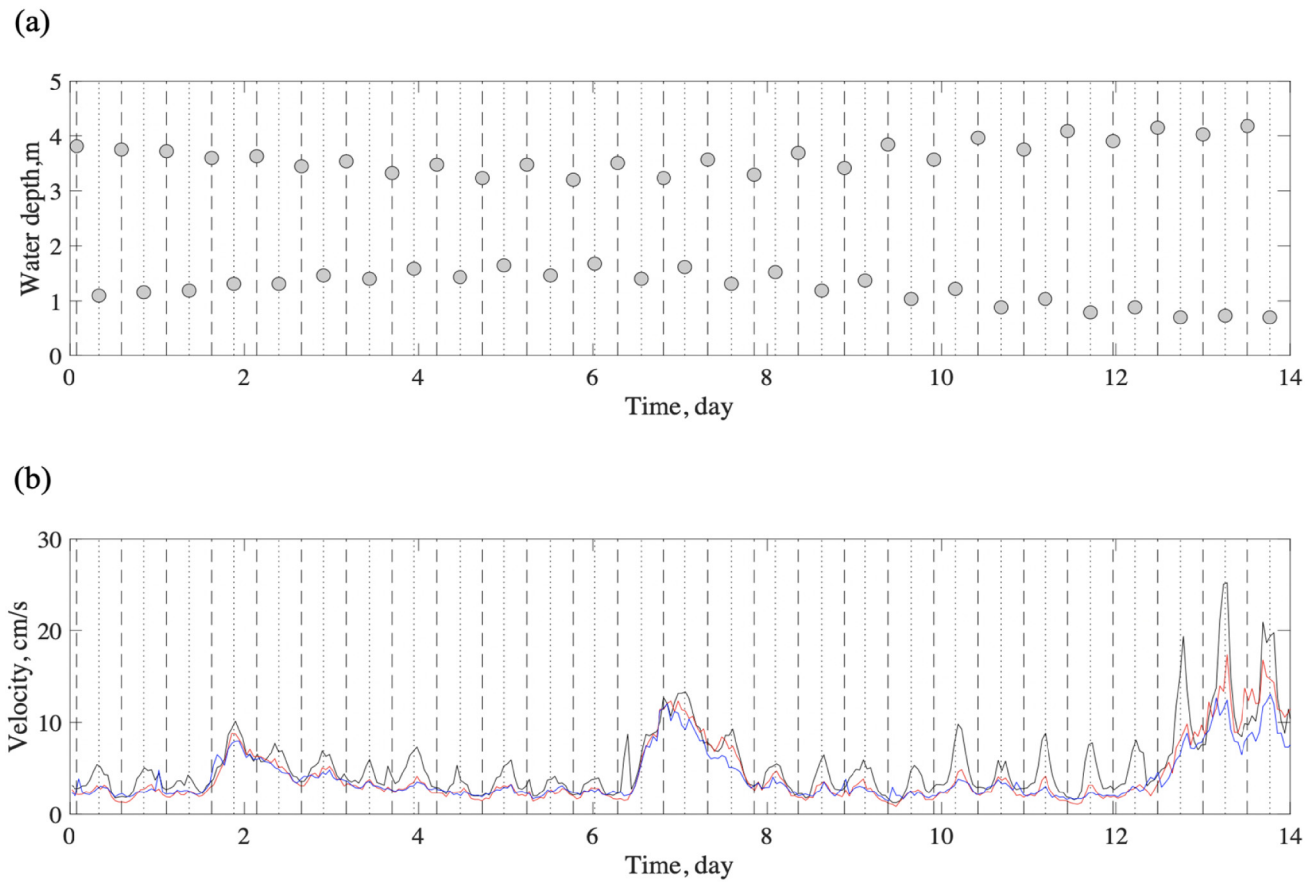


**Fig. 3.** (a) Water depths at the Shallow site at high and low tides, and (b) hourly-averaged $U_{RMS}$ over two weeks. The black curve denotes the Shallow zone (Shallow1). The red curve denotes the Mid zone (Mid2). The blue curve denotes the Deep zone (Deep3). Vertical dotted and dashed lines denote times of low and high tide, respectively.

accretion rate. This was consistent with previous laboratory studies, which found sediment resuspension increased as near-bed *TKE* increased in pure wave and pure current conditions (Tinoco and Coco, 2018; Tang et al., 2019; Zhang et al., 2020). The spatial gradient of *TKE* results in a spatial gradient of exceedance of the critical *TKE* threshold, and therefore a spatial gradient of resuspension. Consistent with this, previous sediment trap measurements within the Nahant meadow indicated significantly higher resuspension both within and adjacent to the meadow in the Shallow zone compared to the other depth zones (data not shown). Assuming sediment supply was the same across the meadow, an increase in resuspension would lead to a lower net sedimentation rate, so that the correlation observed between sedimentation rate and near-bed *TKE* was consistent with the impact of resuspension (Fig. 4).

### 3.3. Sediment organic carbon content and carbon accretion rates

The measured *CAR* values in the Nahant meadow were typical of those observed in other meadows of the same seagrass species. Specifically. previous studies report a range of *CAR* in *Zostera marina L* meadows from 3.1 to 230 g C $m^{-2}$ $yr^{-1}$ (Novak et al., 2020; Poppe and Rybczyk, 2018; Prentice et al., 2020). The *CAR* in the Shallow zone is at the low end of

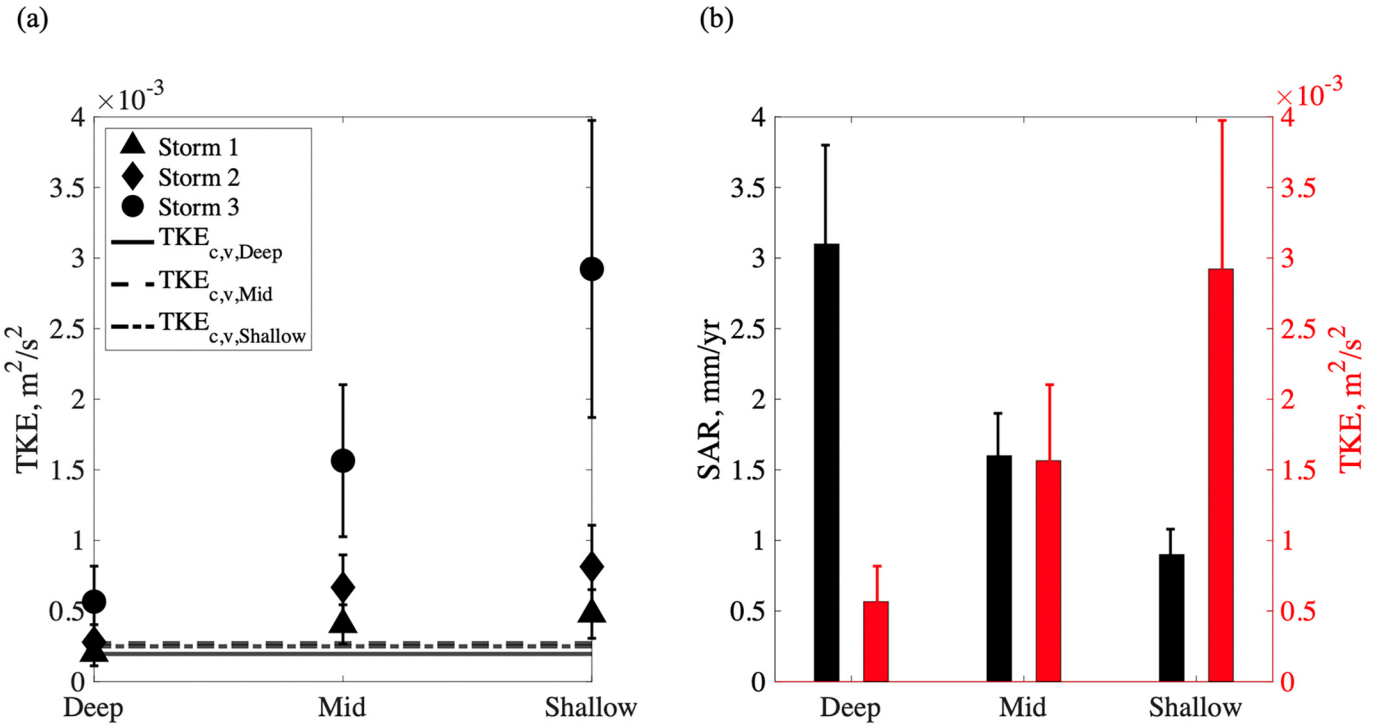


**Fig. 4.** (a) Turbulent kinetic energy (*TKE*) at Deep3, Mid2, and Shallow1 for Storms 1, 2, and 3 (Days 2, 7, and 13 events). The horizontal lines indicate the critical *TKE* thresholds for each meadow site. The thresholds varies between sites due to the different meadow densities, i.e. $n_b$ in Eq. (1). (b) Sediment accretion rate (*SAR*, black bars, left-hand axis) and near-bed turbulent kinetic energy (*TKE*, red bars, right-hand axis) at Deep3, Mid2, and Shallow1 during Storm 3.

this range, while the *CAR* in the Deep zone is close to the average of reported CAR in these studies.

The mean sediment organic carbon fractions (%OC) were statistically significantly different between the Shallow and Mid Zones but not between the Mid and Deep or Shallow and Deep zones (see Fig. B.1 in the Supporting Information). However, differences in sedimentation rates generated differences in *CAR* among all three depth zones. Specifically, *CAR* were statistically significantly different at each depth zone (see Fig. B.2 in the Supporting Information).

Organic carbon accretion might differ between depth zones due to differences in seagrass productivity. For example, Dennison and Alberte (1986) observed that at the deepest sites within a *Zostera marina* L. meadow at Woods Hole, Massachusetts, productivity was controlled by light availability for photosynthesis, whereas light availability was not a major factor in productivity differences in shallower regions of the meadow. However, previous measurements in the Nahant meadow (April to October of 1999 and 2000) did not indicate a dependence of seagrass productivity on water depth (Colarusso, 2006).

Furthermore, the three-fold spatial variation in sediment organic carbon did not have a significant relationship with spatial variation in shoot density, and *CAR* had a negative correlation with shoot density (see Fig. B.3 in the Supporting Information). Specifically, *CAR* was highest where the shoot density was lowest (Table 1). While surprising for autochthonous carbon, this is consistent with allochthonous carbon, which tends to be more significantly influenced by hydrodynamic factors. Recall that Nahant has a significant allochthonous fraction (Fig. 8 in Novak et al., 2020). Specifically, within this wave-dominated meadow, the near-bed velocity, which controls resuspension, has little dependence on local shoot density but instead depends on the integration of shoot density (which determines meadow drag) along the trajectory of the wave. However, shoot density can be an important metric when comparing carbon accretion rates between different meadows. Denser and larger meadows diminish wave energy to a greater degree and thus have a greater ability to curtail resuspension, which would enhance *SAR* and *CAR* (Tang et al., 2019). In contrast to an oscillating wave velocity, a steady current velocity is more directly influenced by a spatial variation in shoot density (e.g., see the discussions in Lowe et al., 2005 and Luhar et al., 2008). Therefore, at current-dominated sites with a patchy meadow structure, one would expect spatial variation in shoot density to be associated with spatial variation in velocity, and thus, potentially, with spatial variation in sediment carbon.

The distance from the meadow edge is another physical factor that can influence the spatial heterogeneity in carbon within a meadow. For example, at a current-dominated site, Oreska et al. (2017) observed that sediment carbon increased with distance from the meadow's leading edge, and they attributed this to the attenuation of current within the meadow due to meadow drag. Specifically, when a current encounters a submerged meadow with a sufficient shoot density, the velocity within the meadow decreases with distance from the leading edge over an adjustment length-scale that is dependent on the meadow height and shoot density (Chen et al., 2013).

At the Nahant site, neither sediment organic carbon nor *CAR* had a significant correlation with distance to the nearest meadow edge, and the highest and lowest *CAR* occurred at similar distances to the nearest edge of the meadow (Fig. 5(a) and (c)). The meadow sites were not within the expected current adjustment length-scale of the meadow (up to 2.5 m, based on Eq. (10) in Chen et al., 2013), such that the distance to the nearest meadow edge was not expected to be a factor. Furthermore, at this wave-dominated site, the distance measured along the direction of wave propagation is more relevant than the distance to the nearest meadow edge. Since the waves transform across the meadow in response to changes in water depth and to dissipation by meadow drag, one should consider the direction of wave propagation and measure the distance from the offshore edge of the meadow. The *CAR* had a significant relationship with distance to the offshore meadow edge (Fig. 5(d)). Specifically, *CAR* decreased with distance from the offshore edge. This was consistent with the increased near-bed wave velocity associated with shoaling, which would tend to produce greater resuspension at sites closer to the shore, which in turn influenced carbon accretion. That is, moving toward shore, the near-bed wave velocity increased, promoting resuspension and diminishing carbon accretion. Consistent with this, Dahl et al. (2018) observed that resuspension removed

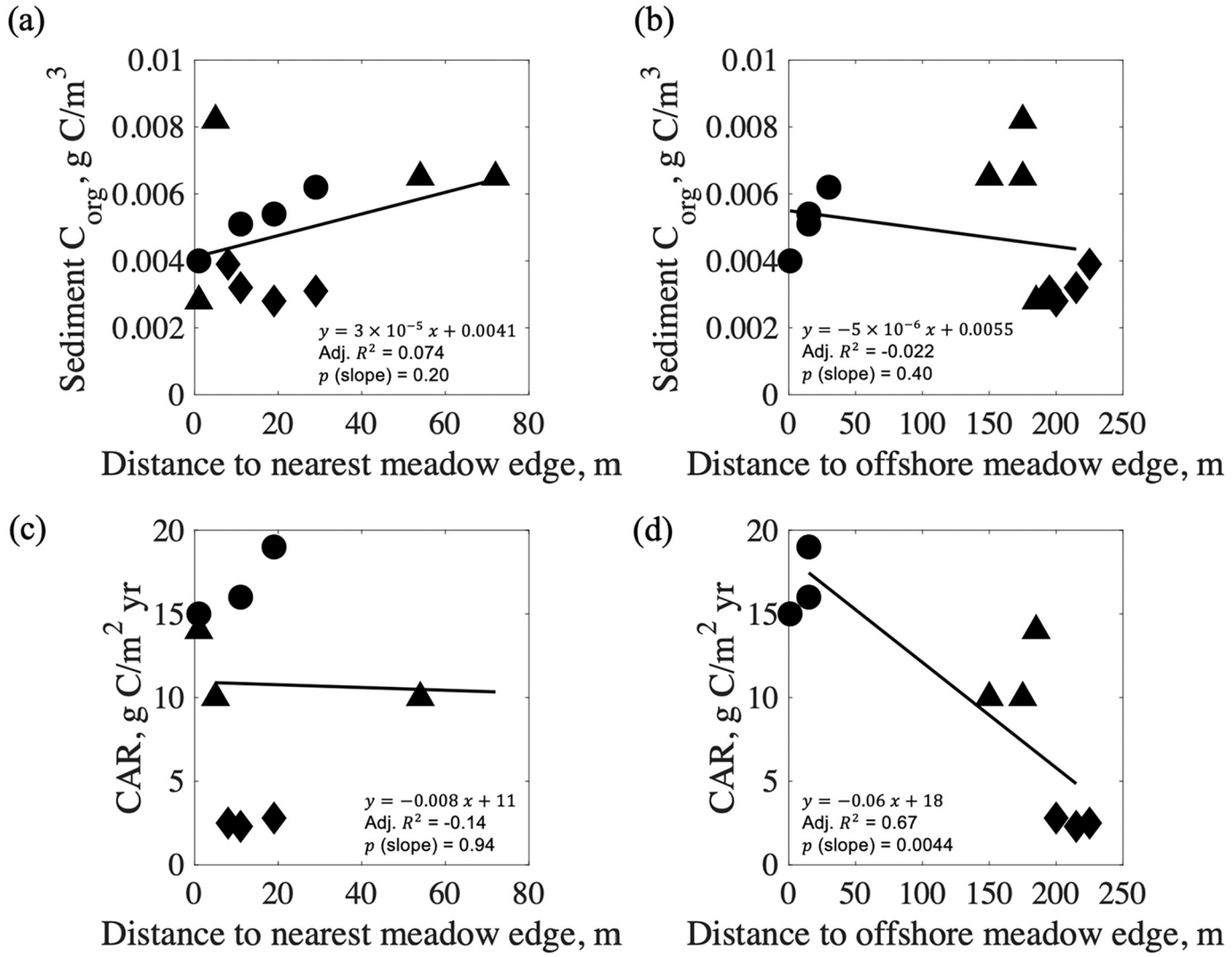


**Fig. 5.** (a,b) Sediment organic carbon and (c,d) carbon accretion rate (*CAR*) versus the distance from nearest meadow edge (a and c) and the distance from offshore meadow edge (b and d). Circles, triangles, and diamonds denote the Deep, Mid, and Shallow zones, respectively. The solid curves denote the lines of best fit.

organic material from the bed within a meadow. Resuspension can also enhance oxygen within the bed, which would tend to diminish carbon retention through increased rates of mineralization by aerobic microbes (e.g., Ståhlberg et al., 2006).

### 3.4. Using hydrodynamic gradients to constrain meadow-scale estimates of carbon

The carbon accretion rates were inversely correlated with hydrodynamic exposure expressed in terms of near-bed *TKE* (Fig. 6), with the following linear best-fit based on Storm 3 (90 % CI, Fig. 6):

$$CAR\left(\frac{g\ C}{m^2 yr}\right) = (-0.69 \pm 0.17)TKE\left(\frac{cm^2}{s^2}\right) + (21 \pm 3). \quad (4)$$

At this wave-dominated site, the near-bed *TKE* can be predicted from wave mechanics. Specifically, wave evolution over the meadow can be described by the conservation of wave energy, including the influence of shoaling and vegetation-induced wave dissipation on the wave amplitude, $a_w$. Bed-induced wave dissipation was assumed to be negligible, compared to vegetation-induced dissipation. Since both shoaling and wave dissipation change with water depth, a marching solution was used to evaluate the wave amplitude at $\Delta x = 1$-m steps across the meadow. Specifically, Eq. (17) in Mendez and Losada (2004) was adapted to describe the change in wave amplitude over the meadow,

$$\frac{a_{w\ (i)}}{a_{w\ (i-1)}} = K_{v\ (i-1)} K_{s\ (i-1)} \quad (5)$$

in which $a_{w(i)}$, $K_{v(i)}$ and $K_{s(i)}$ are the wave amplitude, vegetation dissipation and shoaling coefficients at distance $i$ from the offshore edge of the meadow, respectively, with $i$ corresponding to the progression of 1-m steps ($\Delta x$). The change in wave amplitude due to wave energy dissipation by the meadow can be described as (e.g., Dalrymple et al., 1984)

$$K_{v(i)} = \frac{1}{1 + K_{D(i)} a_{w(i)} \Delta x}, \quad (6)$$

in which the wave decay coefficient

$$K_{D(i)} = \frac{2}{9\pi} C_D n_{b(i)}\ b\ k_{(i)} \frac{9\ sinh\left(k_{(i)} l_{e,m}\right) + sinh\left(3k_{(i)} l_{e,m}\right)}{\left(sinh\left(k_{(i)} D_{(i)}\right)\right)\left(sinh\left(2k_{(i)} D_{(i)}\right) + 2k_{(i)} D_{(i)}\right)} \quad (7)$$

depends on water depth, $D$, wave number, $k$, number of leaves per bed area, $n_b$, and average leaf width, $b$. The drag coefficient $C_D = 2$ for flat leaf morphology (see Luhar and Nepf, 2016). Because seagrass leaves are flexible, their tips can move with the waves, reducing the relative velocity between the leaf and the water, which reduces the drag. The impact of this

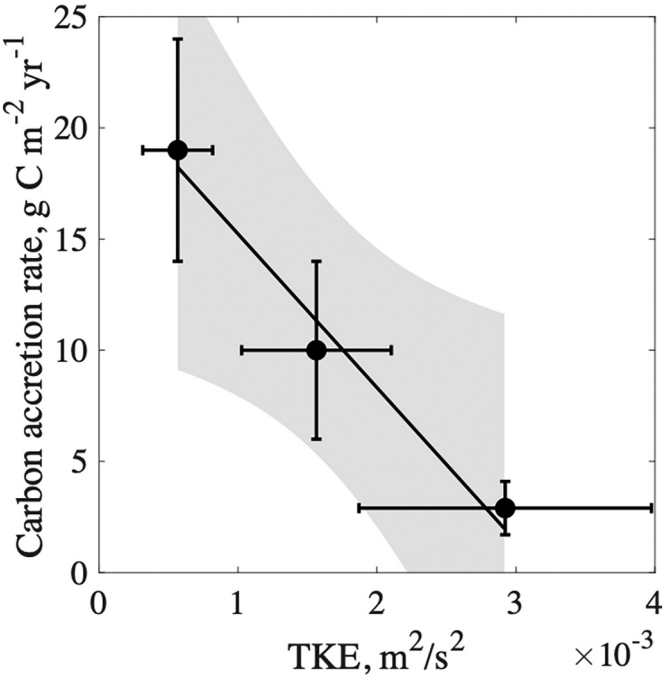


**Fig. 6.** Carbon accretion rate (*CAR*) as a function of near-bed turbulent kinetic energy (*TKE*) during Storm 3. The black curve denotes the linear best fit (Eq. (4)). The shaded region shows the 90 % confidence interval bounds for the fit.

reconfiguration is characterized by the effective meadow height, $l_{e,m}$, which is the height of the meadow that contributes to the drag and wave dissipation. The effective meadow height depends on the morphology and material properties of the leaves and on the wave conditions (Luhar and Nepf, 2016; Luhar et al., 2017). Over a wide range of pure wave conditions, a simple but reasonable approximation for $l_{e,m}$ is 10 % of the average shoot length (see Fig. 5 in Lei and Nepf, 2019).

The group velocity, $C_g$, describes the speed of wave energy propagation (Kamphuis, 2010):

$$C_g = \frac{1}{2}\left(1 + \frac{2kD}{sinh\ (2kD)}\right)\left(\frac{g}{k}\ tanh\ (kD)\right)^{\frac{1}{2}}. \tag{8}$$

As the water depth $D$ decreases, $C_g$ decreases which generally results in an increase in wave amplitude. This is captured by the shoaling coefficient, $K_s$ (Kamphuis, 2010),

$$K_s = \left(\frac{C_{g(i-1)}}{C_{g(i)}}\right)^{\frac{1}{2}}. \tag{9}$$

Based on the bathymetric survey, it was reasonable to assume a linear bottom slope across the meadow (Fig. 1). The leaf density ($n_b$, number of leaves per bed area) was estimated from the shoot density (Table 1) and average number of leaves per shoot in each depth zone; both were assumed to vary smoothly across the meadow and interpolated between measurement sites. The initial wave amplitude at the outer edge of the meadow, $a_{w,0}$, was calculated from linear wave theory and the measured near-bed wave velocity amplitude, $U_w$,

$$U_w = \frac{2\pi}{T} a_w \frac{coshcosh\ (kz)}{sinhsinh\ (kD)}, \tag{10}$$

in which $T$ is the wave period, and $z = 16$ cm was the approximate distance above the bed corresponding to half of the vertical height of the TCM. For this analysis, we focused on Storm 3 conditions. Starting from the offshore edge ($\approx$250 m in Fig. 7), Eq. (5) was evaluated in 1-m increments over the meadow, using Eqs. (6) through (9) to evaluate $K_{v\ (i-1)}$ and $K_{s\ (i-1)}$. Linear wave theory (Eq. (10)) was used to convert the spatial evolution of wave amplitude to spatial variation in near-bed $U_{RMS}$, using $U_{RMS} = U_w/\sqrt{2}$ (Fig. 7(a)). The near-bed $U_{RMS}$ was used in Eq. (1) to estimate near-bed vegetation-generated *TKE* (Fig. 7(b)), assuming a smooth change in shoot density over the meadow. Finally, Eq. (4) was used to predict the spatial variation in carbon accretion rate (Fig. 7(c)). In this way, we used physical models of wave mechanics to interpolate the carbon accretion rate over the meadow. The estimation was made for two wave periods representing the bounds of the measured wave spectral peak ($T = 6$ s and 10 s shown with black and red curves, respectively, in Fig. 7), but the solution was not sensitive to wave periods in this range. Differences between predictions and measurements could be attributed to the assumed linearization of the bathymetry and smooth variation in the meadow structure. In summary, simple modeling tools performed well in predicting the observed spatial variation in hydrodynamic conditions and *CAR*.

Next, we considered the results from Storm 3 (Fig. 7) in the broader context of conditions at the site. The average airport wind speed for August is 4.5 m/s, and the peak hourly airport wind speed on the stormy days (including Storm 3) was 9 m/s. The dominant wind direction is from the southwest, with a fetch of about 5 km. Assuming that the airport wind speeds were representative of the wind speed 10 m above the water surface, we used the fetch-limited Joint North Sea Wave Project (JONSWAP) parameter equations (Kamphuis, 2010) to estimate a significant wave height $H_{m0}$ of 16 cm (using a wind speed of 4.5 m/s) and 33 cm (using a wind speed 9 m/s). Wave heights estimated from the TCM velocity data during the stormy periods were between 20 and 32 cm, confirming that the range of observed conditions were representative of long-term conditions at the site.

To examine the impact of the meadow on the hydrodynamic conditions and *CAR*, we repeated the analysis without vegetation, setting $K_v = 1$ and $n_b = 0$ (Fig. 7(d–f)). Note that at the offshore edge of the meadow ($\approx$ 250 m in Fig. 7) the wave conditions are the same with and without the meadow, because this is the point at which the waves first encounter the meadow. Moving toward shore ($x < 250$ m), the wave velocity and near-bed *TKE* would be significantly higher without the meadow, with wave velocity increasing to more than twice the observed value (Fig. 7(d)). The significant increase in near-bed *TKE* (Fig. 7(e)), suggests that *CAR* would decrease to zero over most of the meadow (based on Eq. (4)), which emphasizes the important role of wave dissipation by the meadow in creating conditions conducive to carbon accretion. We caution that Fig. 7(e) is speculative because Eq. (4) is based on only three points and does not resolve the transition to zero *CAR* at low values of near-bed *TKE*.

The predicted spatial variation in carbon accretion rate $CAR_{(i)}$ (Fig. 7 (c)) was used to calculate the total carbon accretion rate for the meadow, *TCAR*. Again using $\Delta x = 1$ m,

$$TCAR = \Sigma CAR_{(i)}\ \Delta x\ w_{(i)}. \tag{11}$$

$w_{(i)}$ denotes the meadow width at distance $i$ m from Shallow1. The meadow width was assumed to increase linearly from 100 m at Shallow1 to 500 m at Deep3, based on meadow contours developed from boat surveys (Fig. 1). Using Eq. (11), $TCAR = 9.2 \times 10^5$ g C yr$^{-1}$ = 1.0 short tons C·yr$^{-1}$. For comparison, estimates using individual point measurements at the Deep, Mid, and Shallow zones were, respectively, 1.5 short tons C yr$^{-1}$ (50 % higher), 0.80 short tons C yr$^{-1}$ (20 % lower), and 0.20 short tons C yr$^{-1}$ (80 % lower). This comparison demonstrates that individual measurements of *CAR* do poorly in estimating the meadow average, and that the predictable variation in wave velocity over a meadow can constrain estimates of carbon accretion.

Finally, the potential for wave-driven resuspension to generate spatial gradients in *CAR* at other sites can be assessed using wind data and median grain size ($d_{50}$). Wind data and fetch provide an estimate of wave climate at the meadow edge, and the model described above can be used to describe the gradient in wave velocity across the meadow. For resuspension to drive spatial heterogeneity in sediment carbon, two conditions must be

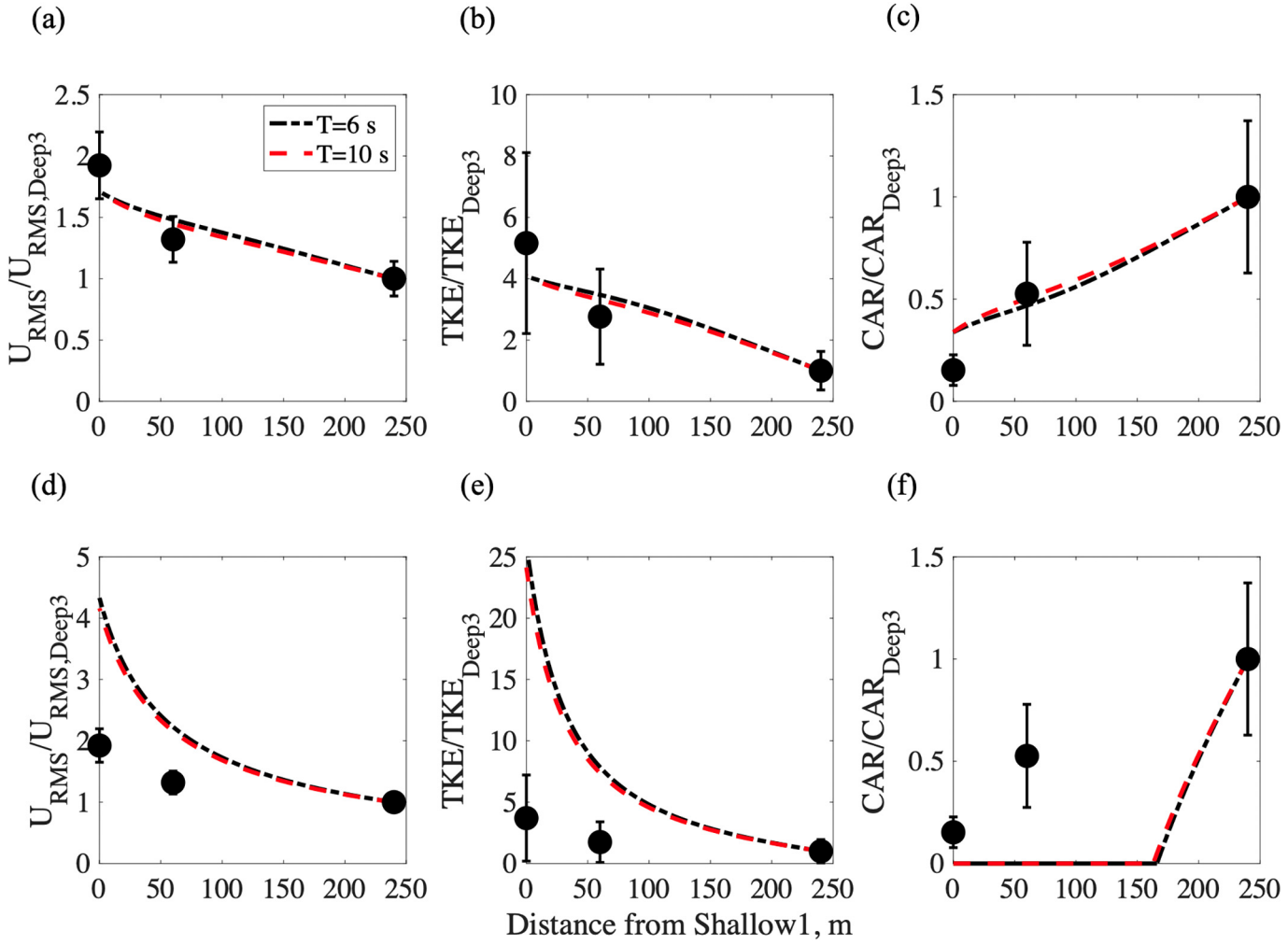


**Fig. 7.** Evolution of (a, d) RMS wave velocity, (b, e) near-bed turbulent kinetic energy (*TKE*), and (c, f) carbon accretion rate (*CAR*) versus distance from the site Shallow1 ($x = 0$) during Storm 3. The top row includes the effects of the meadow on wave dissipation and near-bed *TKE*. The bottom row excludes the impact of the meadow by setting $K_v = 1$ and $n_b = 0$. Black circles represent measurements at Shallow1, Mid2, and Deep3. Dashed curves denote predictions based on physical models and the observed correlation between near-bed *TKE* and carbon accretion (Fig. 6). Two wave periods were considered, $T = 6$ s (black dashed-dotted curve) and $T = 10$ s (red dashed curve), to span the observed range of dominant wave periods at the site.

met. First, there is a gradient in near-bed wave velocity, and thus in near-bed *TKE* within the meadow. Second, the range of *TKE* within the meadow crosses the critical *TKE* threshold for resuspension, so that there will be a gradient in resuspension. The grain size, $d_{50}$, can be used in Eqs. (2) and (3) to infer the critical turbulence level for resuspension. Spatial gradients in resuspension can also be observed with sediment traps.

## 4. Conclusions

Measurements in a *Zostera marina* L. meadow in Nahant Harbor, Massachusetts, showed that spatial variation in sediment and carbon accretion rates correlated with the spatial variation in hydrodynamic intensity, which was characterized by near-bed turbulence. Specifically, sedimentation and carbon accretion rates both decreased as near-bed turbulence increased. This suggested that resuspension driven by turbulence provided a constraint on the rates of accretion. At wave-dominated sites, near-bed turbulence estimated from wave velocity and meadow morphology may provide a framework for describing spatial heterogeneity in carbon accretion and carbon sequestration within seagrass meadows, which could facilitate more accurate carbon measurements. More accurate carbon measurements could advance carbon credit assessment methods and improve the design of targeted seagrass conservation and restoration projects.

## CRediT authorship contribution statement

**Jiarui Lei:** Conceptualization, Methodology, Investigation, Formal analysis, Visualization, Writing – original draft, Writing – review & editing. **Rachel Schaefer:** Methodology, Investigation, Formal analysis, Visualization, Writing – original draft, Writing – review & editing. **Phil Colarusso:** Conceptualization, Methodology, Resources, Investigation, Writing – review & editing. **Alyssa Novak:** Conceptualization, Methodology, Resources, Investigation, Writing – review & editing. **Juliet C. Simpson:** Conceptualization, Methodology, Resources, Investigation, Writing – review & editing. **Pere Masqué:** Methodology, Writing – review & editing. **Heidi Nepf:** Conceptualization, Methodology, Resources, Funding acquisition, Investigation, Formal analysis, Visualization, Writing – review & editing, Supervision, Project administration.

## Data availability

Data will be made available on request.

## Declaration of competing interest

The authors declare that they have no known competing financial interests or personal relationships that could have appeared to influence the work reported in this paper.

## Acknowledgements

This study was supported by Shell International Exploration and Production through the MIT Energy Initiative. R. Schaefer was supported in part by the National Science Foundation Graduate Research Fellowship under Grant No. 1745302. We thank the U.S. Environmental Protection Agency dive team for their assistance in the field: Brent England, Jean Brochi, Chuck Protzmann, and Eric Nelson. The bathymetry and meadow mapping were collected by Mike Sacarny and Juliet C. Simpson under award NA18OAR4170105 from the National Sea Grant College Program of the U.S. Department of Commerce's National Oceanic and Atmospheric Administration. The International Atomic Energy Agency is grateful for the support provided by the Government of the Principality of Monaco. Ved Ahuja assisted with processing sediment samples at Boston University.

## Appendix A. Supplementary data

Supplementary data to this article can be found online at https://doi.org/10.1016/j.scitotenv.2022.158685.

## References

Arias-Ortiz, A., Masqué, P., Garcia-Orellana, J., Serrano, O., Mazarrasa, I., Marbà, N., Lovelock, C., Lavery, P., Duarte, C.M., 2018. Reviews and syntheses: 210Pb-derived sediment and carbon accumulation rates in vegetated coastal ecosystems – setting the record straight. Biogeosciences 15, 6791–6818. https://doi.org/10.5194/bg-15-6791-2018.

Chen, Z., Jiang, C., Nepf, H., 2013. Flow adjustment at the leading edge of a submerged aquatic canopy. Water Resour. Res. 49 (9), 5537–5551. https://doi.org/10.1002/wrcr.20403.

Colarusso, Phil, 2006. Natural and Stress Induced Changes in Non-structural Carbohydrate Concentrations in Eelgrass (Zostera marina L.). Northeastern University Doctoral dissertation.

Dahl, M., Infantes, E., Clevesjö, R., Linderholm, H.W., Björk, M., Gullström, M., 2018. Increased current flow enhances the risk of organic carbon loss from Zostera marina sediments: insights from a flume experiment. Limnol. Oceanogr. 63 (6), 2793–2805. https://doi.org/10.1002/lno.11009.

Dalrymple, R.A., Kirby, J.T., Hwang, P.A., 1984. Wave diffraction due to areas of energy dissipation. J. Waterw. Port Coast. Ocean Eng. 110 (1), 67–79. https://doi.org/10.1061/(ASCE)0733-950X(1984)110:1(67).

Dennison, W.C., Alberte, R.S., 1986. Photoadaptation and growth of Zostera marina L. (eelgrass) transplants along a depth gradient. J. Exp. Mar. Biol. Ecol. 98, 265–282. https://doi.org/10.1016/0022-0981(86)90217-0.

Duarte, C.M., Marbà, N., Gacia, E., Fourqurean, J.W., Beggins, J., Barrón, C., Apostolaki, E.T., 2010. Seagrass community metabolism: assessing the carbon sink capacity of seagrass meadows. Glob. Biogeochem. Cycles 24 (4), 1–8. https://doi.org/10.1029/2010GB003793.

Fonseca, M.S., Cahalan, J.A., 1992. A preliminary evaluation of wave attenuation by 4 species of seagrass. Estuar. Coast. Shelf Sci. 35 (6), 565–576. https://doi.org/10.1016/S0272-7714(05)80039-3.

Fourqurean, J.W., Duarte, C.M., Kennedy, H., Marbà, N., Holmer, M., Mateo, M.A., Apostolaki, E.T., Kendrick, G.A., Krause-Jensen, D., Serrano, O., 2012. Seagrass ecosystems as a globally significant carbon stock. Nat. Geosci. 5, 505–509. https://doi.org/10.1038/ngeo1477.

Gacia, E., Duarte, C., 2001. Sediment retention by a Mediterranean Posidonia oceanica meadow: the balance between deposition and resuspension. Estuar. Coast. Shelf Sci. 52, 505–514. https://doi.org/10.1006/ecss.2000.0753.

Gacia, E., Granata, T., Duarte, C., 1999. An approach to measurement of particle flux and sediment retention within seagrass (Posidonia oceanica) meadows. Aquat. Bot. 65, 255–268. https://doi.org/10.1016/S0304-3770(99)00044-3.

Granata, T., Serra, T., Colomer, J., Casamitjana, X., Duarte, C., Gacia, E., 2001. Flow and particle distributions in a nearshore seagrass meadow before and after a storm. Mar. Ecol. Prog. Ser. 218, 95–106. https://doi.org/10.3354/meps218095.

Gruber, R., Kemp, W.M., 2010. Feedback effects in a coastal canopy-forming submersed plant bed. Limnol. Oceanogr. 55 (6), 2285–2298. https://doi.org/10.4319/lo.2010.55.6.2285.

Howard, J., Hoyt, S., Isensee, K., Pidgeon, E., Telszewski, M., 2014. Coastal blue carbon: methods for assessing carbon stocks and emissions factors in mangroves, tidal salt marshes, and seagrass meadows. Conservation International, Intergovernmental Oceanographic Commission of UNSECO, International Union for Conservation of Nature.

Infantes, E., Orfila, A., Simarro, G., Terrados, J., Luhar, M., Nepf, H., 2012. Effect of a seagrass (Posidonia oceanica) meadow on wave propagation. Mar. Ecol. Prog. Ser. 456, 63–72. https://doi.org/10.3354/meps09754.

Kamphuis, J.William, 2010. Introduction to coastal engineering and management. Advanced Series on Ocean Engineering. Vol. 30. Word Scientific Co. Pte. Ltd.

Kennedy, H., Beggins, J., Duarte, C., Fourqurean, J., Holmer, M., Marbà, N., Middelburg, J., 2010. Seagrass sediments as a global carbon sink: isotopic constraints. Glob. Biogeochem. Cycles 24, GB4026. https://doi.org/10.1029/2010GB003848.

Keulegan, G.H., Carpenter, L.H., 1958. Forces on cylinders and plates in an oscillating fluid. J. Res. Natl. Bur. Stand. 60 (5), 423–440. https://doi.org/10.6028/jres.060.043.

Komar, P.D., Miller, C.M., 1973. The threshold of sediment movement under oscillatory water waves. J. Sediment. Petrol. 43 (4), 1101–1110. https://doi.org/10.1306/74D7290A-2B21-11D7-8648000102C1865D.

Krishnaswami, S., Lal, D., Martin, J.M., Meybeck, M., 1971. Geochronology of lake sediments. Earth Planet. Sci. Lett. 11, 407–414. https://doi.org/10.1016/0012-821X(71)90202-0.

Lavery, P., Mateo, M., Serrano, O., Rozaimi, M., 2013. Variability in the carbon storage of seagrass habitats and its implications for global estimates of blue carbon ecosystem service. PLoS One 8 (9), e73748. https://doi.org/10.1371/journal.pone.0073748.

Lei, J., Nepf, H., 2019. Wave damping by flexible vegetation: connecting individual blade dynamics to the meadow scale. Coast. Eng. 147, 138–148. https://doi.org/10.1016/j.coastaleng.2019.01.008.

Lei, J., Nepf, H., 2021. Evolution of velocity from leading edge of 2D and 3D submerged canopies. J. Fluid Mech. 916, 1–37. https://doi.org/10.1017/jfm.2021.197.

Lowe, R.J., Koseff, J.R., Monismith, S.G., 2005. Oscillatory flow through submerged canopies: 1. Velocity structure. J. Geophys. Res. Oceans 110 (C10). https://doi.org/10.1029/2004JC002788.

Luhar, M., Nepf, H.M., 2016. Wave-induced dynamics of flexible blades. J. Fluids. Struct. 61, 20–41. https://doi.org/10.1016/j.jfluidstructs.2015.11.007.

Luhar, M., Rominger, J., Nepf, H., 2008. Interaction between flow, transport and vegetation spatial structure. Environ. Fluid Mech. 8, 423–439. https://doi.org/10.1007/s10652-008-9080-9.

Luhar, M., Infantes, E., Nepf, H.M., 2017. Seagrass blade motion under waves and its impact on wave decay. J. Geophys. Res. Ocean 122, 3736–3752. https://doi.org/10.1002/2017JC012731.

Mendez, F.J., Losada, I.J., 2004. An empirical model to estimate the propagation of random breaking and nonbreaking waves over vegetation fields. Coast. Eng. 51, 103–118. https://doi.org/10.1016/j.coastaleng.2003.11.003.

Novak, A.B., Pelletier, M.C., Colarusso, P., Simpson, J., Gutierrez, M.N., Arias-Ortiz, A., Charpentier, M., Masqué, P., Vella, P., 2020. Factors influencing carbon stocks and accumulation rates in eelgrass meadows across New England, USA. Estuar. Coast. 43 (8), 2076–2091. https://doi.org/10.1007/s12237-020-00754-9.

Oreska, M.P.J., McGlathery, K.J., Porter, J.H., 2017. Seagrass blue carbon spatial patterns at the meadow-scale. PLoS One 12. https://doi.org/10.1371/journal.pone.0176630.

Poppe, K.L., Rybczyk, J.M., 2018. Carbon sequestration in a pacific northwest eelgrass (Zostera marina) meadow. Northwest Sci. 92 (2), 80–91. https://doi.org/10.3955/046.092.0202.

Prentice, C., Poppe, K.L., Lutz, M., Murray, E., Stephens, T.A., Spooner, A., Hessing-Lewis, M., Sanders-Smith, R., Rybczyk, J.M., Apple, J., Short, F.T., Gaeckle, J., Helms, A., Mattson, C., Raymond, W.W., Klinger, T., 2020. A synthesis of blue carbon stocks, sources, and accumulation rates in eelgrass (Zostera marina) meadows in the Northeast Pacific. Glob. Biogeochem. Cycles 34 (2), 1–16. https://doi.org/10.1029/2019GB006345.

Ricart, A.M., York, P.H., Bryant, C.V., Rasheed, M.A., Ierodiaconou, D., Macreadie, P.I., 2020. High variability of blue carbon storage in seagrass meadows at the estuary scale. Sci. Rep. 10, 1–12. https://doi.org/10.1038/s41598-020-62639-y.

Sanchez-Cabeza, J.A., Masqué, P., Ani-Ragolta, I., 1998. 210Pb and 210Po analysis in sediments and soils by microwave acid digestion. J. Radioanal. Nuc. Chem. 227, 19–22. https://doi.org/10.1007/BF02386425.

Serrano, O., Lavery, P.S., Rozaimi, M., Mateo, M.Á., 2014. Influence of water depth on the carbon sequestration capacity of seagrasses. Glob. Biogeochem. Cycles 28 (9), 950–961. https://doi.org/10.1002/2014GB004872.

Ståhlberg, C., Bastviken, D., Svensson, B.H., Rahm, L., 2006. Mineralisation of organic matter in coastal sediments at different frequency and duration of resuspension. Estuar. Coast. Shelf Sci. 70 (1–2), 317–325. https://doi.org/10.1016/j.ecss.2006.06.022.

Tang, C., Lei, J., Nepf, H.M., 2019. Impact of vegetation-generated turbulence on the critical, near-bed, wave-velocity for sediment resuspension. Water Resour. Res. 55 (7), 5904–5917. https://doi.org/10.1029/2018WR024335.

Tanino, Y., Nepf, H.M., 2008. Lateral dispersion in random cylinder arrays at high Reynolds number. J. Fluid Mech. 600, 339–371. https://doi.org/10.1017/S0022112008000505.

Tinoco, R.O., Coco, G., 2018. Turbulence as the main driver of resuspension in oscillatory flow through vegetation. J. Geophys. Res. Earth Surf. 123, 891–904. https://doi.org/10.1002/2017JF004504.

Zhang, Y., Tang, C., Nepf, H., 2018. Turbulent kinetic energy in submerged model canopies under oscillatory flow. Water Resour. Res. 54 (3), 1734–1750. https://doi.org/10.1002/2017WR021732.

Zhang, J., Lei, J., Huai, W., Nepf, H., 2020. Turbulence and particle deposition under steady flow along a submerged seagrass meadow. J. Geophys. Res. Oceans 125 (5). https://doi.org/10.1029/2019JC015985.